Supplementary Materials: Soft X-Ray Second Harmonic Generation as an Interfacial Probe

R. K. Lam,[1,2] S. L. Raj,[1,2] T. A. Pascal,[3] C. D. Pemmaraju,[4] L. Foglia,[5] A. Simoncig,[5] N. Fabris,[6,7] P. Miotti,[6,7] C. J. Hull,[1,2] A. M. Rizzuto,[1,2] J. W. Smith,[1,2] R. Mincigrucci,[5] C. Masciovecchio,[5] A. Gessini,[5] E. Allaria,[5] G. De Ninno,[5,8] B. Diviacco,[5] E. Roussel,[5] S. Spampinati,[5] G. Penco,[5] S. Di Mitri,[5] M. Trovò,[5] M. Danailov,[5] S. T. Christensen,[9] D. Sokaras,[10] T.-C. Weng,[11] M. Coreno,[5,12] L. Poletto,[6] W. S. Drisdell,[2] D. Prendergast,[3] L. Giannessi,[5,13] E. Principi,[5] D. Nordlund,[10] R. J. Saykally,[1,2] and C. P. Schwartz[3,10]

[1] *Department of Chemistry, University of California, Berkeley, California 94720, USA*
[2] *Chemical Sciences Division, Lawrence Berkeley National Laboratory, Berkeley, California 94720, USA*
[3] *The Molecular Foundry, Lawrence Berkeley National Laboratory, Berkeley, California 94720, USA*
[4] *Theory Institute for Materials and Energy Spectroscopies, SLAC National Accelerator Laboratory, Menlo Park, California 94025, USA*
[5] *Elettra-Sincrotrone Trieste S.C.p.A., Strada Statale 14 - km 163.5, 34149 Trieste, Italy*
[6] *Institute of Photonics and Nanotechnologies, National Research Council of Italy, via Trasea 7, I-35131 Padova, Italy*
[7] *Department of Information Engineering, University of Padova, via Gradenigo 6/B, I-35131 Padova, Italy*
[8] *Laboratory of Quantum Optics, University of Nova Gorica, 5001 Nova Gorica, Slovenia*
[9] *National Renewable Energy Laboratory, Golden, Colorado, 80401, USA*
[10] *SLAC National Accelerator Laboratory, Menlo Park, California 94025, USA*
[11] *Center for High Pressure Science & Technology Advanced Research, Pudong, Shanghai 201203, China*
[12] *ISM-CNR, Elettra Laboratory, Basovizza; I-34149 Trieste, Italy*
[13] *ENEA, C.R. Frascati, Via E. Fermi 45, 00044 Frascati (Rome), Italy*

SAMPLES

Unsupported nanocrystalline graphite thin films (thickness: 100, 300, 500, 720 nm), mounted onto L1.0 rings (10 mm diameter), were purchased from Lebow Company (Goleta, CA).

EXPERIMENTAL DESIGN

The soft x-ray SHG experiment was performed at EIS-TIMEX end-station of the Elastic and Inelastic Scattering (EIS) beamline [1, 2] at the FERMI FEL-2 free electron laser [3, 4]. FEL-2 is based on a double high gain harmonic generation (HGHG) conversion scheme. The HGHG scheme consists in preparing the electron beam phase space in a first undulator (modulator), where the interaction with an external laser (seed) induces a controlled and periodic modulation in the beam longitudinal energy distribution. The beam propagates through a dispersive section converting the energy modulation into a density modulation. The density modulated beam is then injected in a long undulator (amplifier) where the FEL amplification process is enhanced by the presence of the modulation. This sequence is repeated twice in FERMI FEL-2 in order to achieve high harmonic multiplication factors [4]. The input seed used in this experiment corresponds to the third harmonic of a Ti:Sa oscillator followed by a regenerative amplifier. A further pulse temporal compression stage was set up in the UV to reduce the duration of the seed to 67 fs.

TABLE S1: FERMI FEL pulse characteristics: wavelength (nm), harmonic number, Fourier limited spectral width (σ, nm), measured spectral width (σ, nm), coherence length (μm) and number of shots for various data sets.

Wavelength (nm)	$n\ x\ m$	Estimated duration (FWHM, fs)	Fourier limited spectral width (σ, nm)	Measured (most probable) spectral width (σ, nm)	Coherence length (FWHM, μm)	Shots
4.02	65	22.7	$4.5 \cdot 10^{-4}$	$1.1 \cdot 10^{-3}$	2.7	3398
4.36	60	23.3	$5.1 \cdot 10^{-4}$	$2.0 \cdot 10^{-3}$	1.8	794
4.76	55	24	$5.9 \cdot 10^{-4}$	$2.2 \cdot 10^{-3}$	1.9	479

When the FEL is optimized for maximizing the peak power, in the HGHG process the frequency upshift to harmonic n typically shortens the output pulse by a factor $\sim 7/(6n^{1/3})$ [5]. The three wavelengths used in the experiment

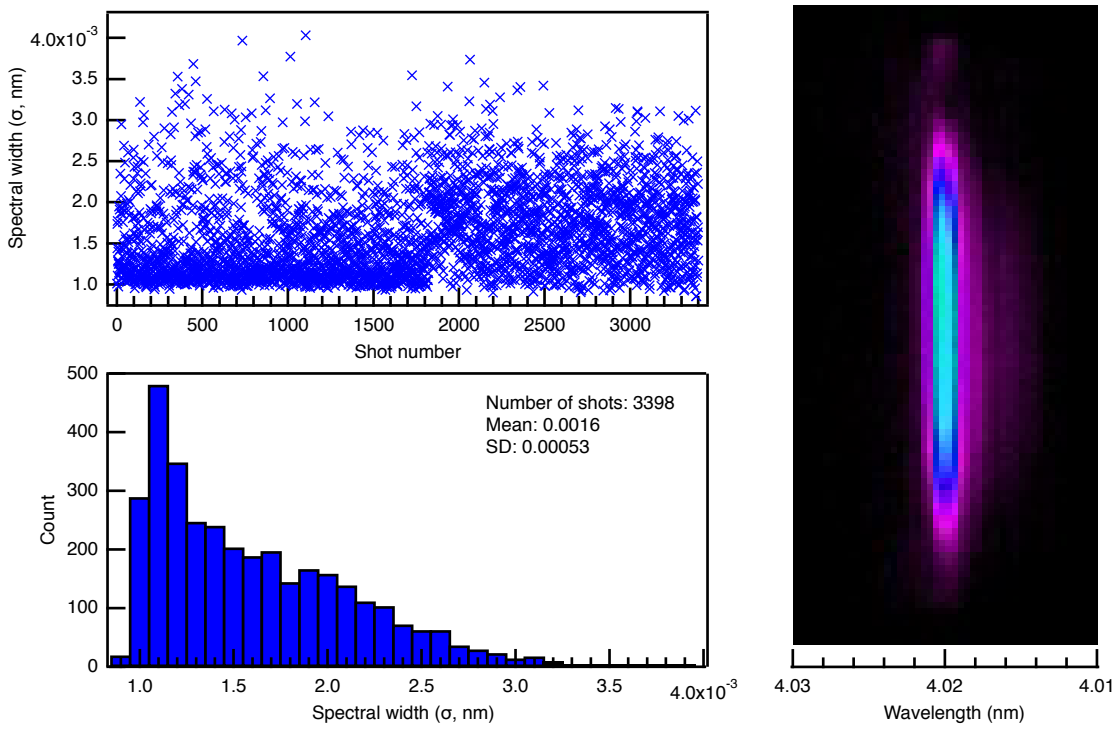

FIG. S1: Spectral width. Top left: Spectral width (σ, nm) vs. shot number for the 3398 shots in the histogram. Bottom left: Histogram of the FEL spectral width (σ, nm) at 4.02 nm. The most probable value is $1.1 \cdot 10^{-4}$ nm. Right: Single shot of the FEL at 4.02 nm with spectral spread along the horizontal axis (nm).

correspond to the conversion of the seed to harmonic orders n = 11th, 12th, and 13th in the first stage, and harmonic m = 5 in the second. We may therefore estimate the pulse shortening corresponding to the double stage conversion of FEL-2 as $(7/6)^2/(nm)^{1/3}$. We have listed the duration estimate for the three wavelengths in Table S1, together with the measured spectral width, the expected width for Gaussian Fourier transform limited pulses, and the corresponding coherence length. The spectral width was measured as the most probable value resulting from the statistical analysis of >450 shots at a given wavelength. An example is shown in Fig. S1, where a typical histogram of the spectral width (σ, nm) is shown at n=13, m=5.

The graphite films were attached to a 5-axis manipulator stage. The sample was rastered (∼50–60 μm) so that pristine graphite was probed with each laser shot, mitigating the effects of sample damage. Between laser shots, the positioning of the sample stage, monitored by a telemicroscope, was moved along the beam axis to ensure that the sample was always at the focal point of the ellipsoidal mirror.

Photons from the FEL source are transported to the endstation along the Photon Analysis, Delivery, and Reduction System (PADReS) [6], which also provided shot-to-shot photon diagnostics (I_0 monitor, PRESTO (Pulse-Resolved Energy Spectrometer (Transparent and Online))) and a gas attenuator (6 m, N_2, 1.7 mbar) to remove the first stage FERMI radiation. The FEL beam was passed through an iris (2 mm) to attenuate both the off-axis second harmonic emission from the FEL light source and the emission of the first undulator chain of FERMI characterized by a larger divergence, and focused by an ellipsoidal mirror (f = 1.4 m) onto the graphite sample at normal incidence. The transmitted beam and the collinear second harmonic signal were then passed through a 600 nm Al filter to attenuate the fundamental beam, and into an EUV spectrometer [7]. In the spectrometer, the beam was reflected from a grating (Hitachi cod. 001-0450, 2400 gr/mm central groove density) in first order – to separate the second harmonic signal from the fundamental – and onto a CCD (Princeton Instruments PIXIS-XO 400 B). A single CCD image was recorded for each laser pulse.

To explicitly separate the relative contributions to the measured second harmonic signal from the FEL source and the sample, measurements were also made without the sample present. In general, an approximately equal number of laser shots were recorded with and without the graphite sample present. These off-sample measurements also allowed for the direct characterization of the FEL beam (intensity, mode hopping, etc.).

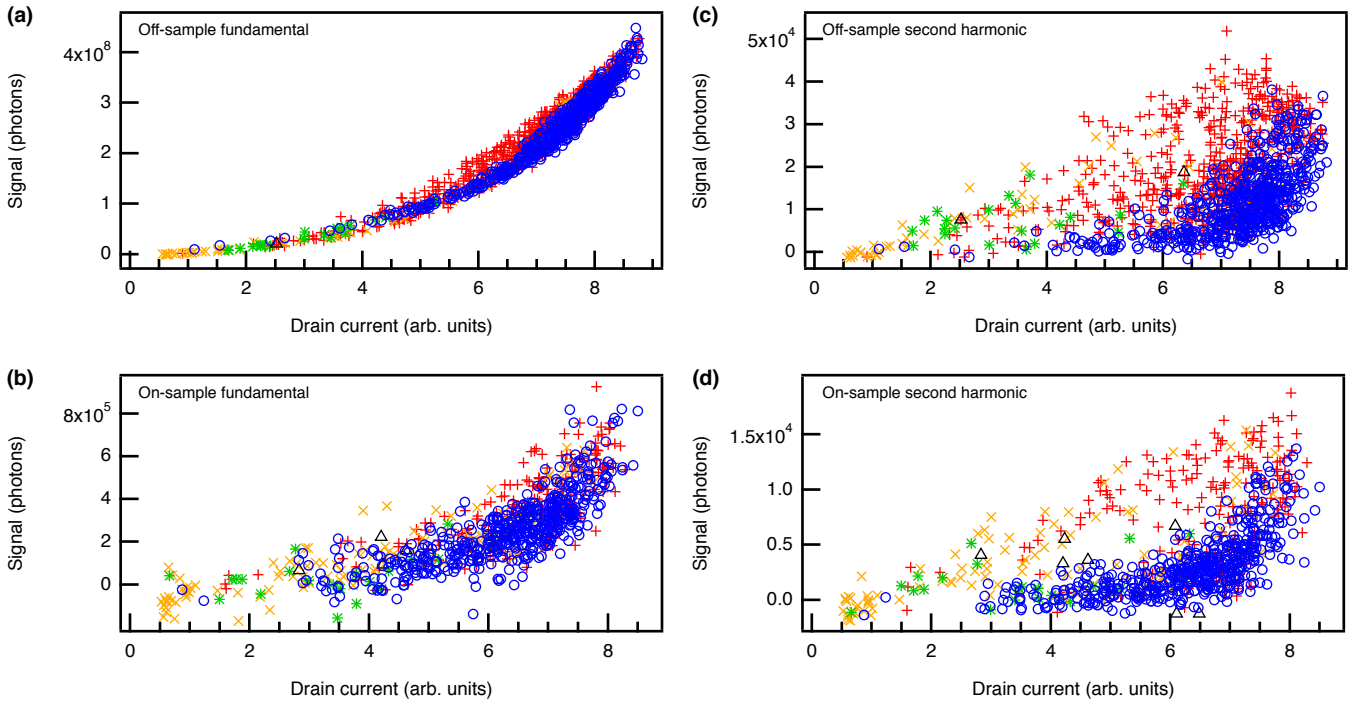

FIG. S2: Pulse energy calibration and filtering. The correlation between the drain current (arb. units) and spectrometer signal for the off-sample fundamental (a) were used to calibrate the FEL pulse energy. Signals measured on the CCD were filtered using a series of four steps: 1) low energy cutoff (not shown), 2) horizontal (orange X; σ, nm) and vertical (red +; σ, mm) beam profiles, 3) FWHM (green $*$), 4) distance, remaining outliers (black $\triangle$). The points remaining after filtering are shown as blue circles. The uncalibrated dataset presented is from the 500 nm graphite sample at 307.86 eV (4.02 nm). (a) Off-sample fundamental (b) On-sample fundamental (c) Off-sample second harmonic (d) On-sample second harmonic.

DATA ANALYSIS

Each dataset for every graphite sample at each photon energy (260.49 eV, 284.18 eV, and 307.86 eV) contained >250 FEL pulses. The signal recorded on the CCD at the fundamental and second harmonic wavelengths is shown in Fig. S2 for a single data set. Figure S2 shows data from the 500 nm graphite sample at 307.86 eV (4.02 nm). Each plotted point represents a single laser shot and its corresponding signal on the CCD, scaling only for the spectrometer efficiency and the transmission through the 600 nm Al filter before the spectrometer, with respect to the uncalibrated drain current measured off the ellipsoidal mirror immediately upstream of the sample. The correlation between the drain current and the CCD signal were used to calibrate the FEL pulse energies. In these data, it is readily apparent that mode stability of the FERMI light source was of particular concern and is especially evident in the signal at the second harmonic wavelengths. This instability may be caused by two main factors, which may also play a concurrent role. The central wavelength depends on the slope of the beam longitudinal energy distribution. A change in this slope, dependent on the temporal jitter between seed and the electron bunch at the first modulator, may lead to a periodic shift and broadening of the spectrum. A second aspect is related to the FEL tuning condition. Seeking the maximum pulse energy may bring one of the FEL amplifiers to a pre-saturation condition where the pulse duration scaling no longer holds. Under this condition, the pulse may develop side-bands and split into two satellites. The energy extracted increases, but this increase is generally not accompanied by a growth of the peak power.

Filtering and removing contributions from the undesired modes was necessary. This filtering was accomplished in a series of automated steps utilizing the photon diagnostic data from PADReS and the image from the CCD in the spectrometer acquired for each laser pulse. Initially, a low pulse energy cutoff was applied, removing data points originating from FEL pulses for which the measured drain current on the ellipsoidal mirror was less than 0.5 arb. units (not shown in figure). The data were then filtered utilizing the horizontal (energy distribution) and vertical (spatial spread) beam profiles measured by the PADReS spectrometer and the full width half maximum (FWHM) of

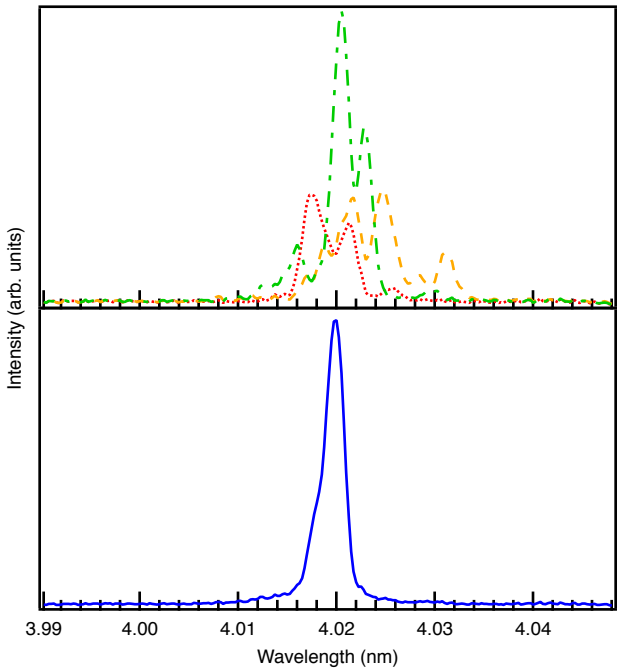

FIG. S3: Spectral profile of FEL pulses. Typical spectra of pulses removed by filtering (top, dashed lines) vs pulses remaining after filtering (bottom, blue).

the peak corresponding to the fundamental beam in the projection of the CCD image along the energy axis. Points were removed from the dataset if the standard deviation (σ) was greater than 0.006 nm or less than 0.58 mm for the horizontal and vertical profiles, respectively. Note that when the FEL enters a regime wherein spectral splitting occurs, a spatial narrowing of the pulse is also observed. For the FWHM filtering, points were removed if they were determined to be outliers with respect to the remaining dataset following the removal of points by the horizontal and vertical profile filtering. Finally, the remaining outliers, determined by a distance filter, were removed. The distance filter was implemented by renormalizing the pulse energy and signal axes (min: 0, max: 1) and calculating the distance between the points and (0.2, 0.75). The distribution of distances was then used in the determination of the outliers. Outliers were determined using a simple box plot model wherein an outlier was defined as those points lying beyond the whiskers 1.5xIQR (interquartile range) below or above the first and third quartile, respectively. Examples of pulses removed by and remaining after filtering are shown in Fig. S4.

Following the filtering, the remaining points were binned. As the sampling of pulse energies were not uniform, the bin positions were determined by the centroid of the dataset. The appropriate scaling factors were then applied to account for attenuation through the graphite sample and for the portion of the signal blocked by the entrance slits to the spectrometer. The proportion of the signal blocked by the spectrometer entrance slits was determined using the spatial profile of the fundamental beam on the spectrometer, along with the size of the horizontal and vertical entrance slits. From this, utilizing the shadow cast on the CCD from the slits, the percentage of the flux transmitted through the slits can be calculated, providing a direct measurement of the fundamental beam intensity. The difference between the on- and off-sample curves then yields the power dependence curves shown in Fig. 2.

THEORETICAL METHODS

First-principles density functional theory (DFT) [8, 9] simulations were carried out using the `exciting` [10] all-electron full-potential computer package which employs (linearized) augmented planewave + local orbital [(L)APW+lo] methods. In order to investigate second harmonic generation at the (0001) surface of graphite, a supercell comprising of an eight-layer slab of AB stacked hexagonal graphite was set up (see Fig. 3d). The slab model was generated via a 1x1x4 repetition of a unit cell of AB stacked graphite with the experimentally determined [11] in-plane and out-of-plane lattice parameters: 2.464 Å and 6.711 Å, respectively. A vacuum region of 10 Å was chosen to separate periodic images of the slab along the z direction perpendicular to the slab surface. No additional geometry opti-

mization was carried out as previous DFT calculations [12] of the (0001) surface have indicated insignificant surface relaxation with interlayer separation at the surface very similar to the bulk value. The parameter rgkmax, which represents the product of the minimum muffin-tin radius and maximum length of **G+k** vectors in the basis, was set to 7. The Brillouin zone of the two-dimensional slab was sampled using a 30x30x1 Γ-centered k-point grid. Exchange correlation effects within DFT were modeled at the level of the Perdew-Zunger Local Density Approximation (LDA) [13]. In order to facilitate response calculations near C K edge frequencies, the $1s$ core-orbitals of carbon were explicitly included in the valence self-consistent field treatment so that their Kohn-Sham eigenvalues and eigenvectors are self-consistently updated within the simulation.

To calculate the second-order susceptibility tensor relevant to SHG at the C K edge, we employed the second-order response formalism from Sharma *et al.* [14] which is implemented within `exciting` [10]. Within this approach, the second-order susceptibility $X^{(2)}(2\omega, \omega, \omega)$ involves contributions arising from excitation energies resonant with ω as well as 2ω (see equations 49-51 of Sharma et al.) [14]. We employ the independent particle approximation, wherein the excitation energy ω_{mn} between electronic states m and n ($m \neq n$) is given by $\omega_{mn} = \varepsilon_m - \varepsilon_n$ where ε_m, ε_n are their respective Kohn-Sham eigenvalues. The linear spectrum was calculated within the same non-interacting formalism to be consistent. Since C $1s$ core electrons are situated ∼280 eV below the Fermi energy, for excitation energies at the C K edge, ω is roughly 280 eV. Therefore, in order to capture contributions to involving C $1s$ excitations resonant near 2ω, we included 2400 empty Kohn-Sham eigenstates whose energies extend up to ∼320 eV above the Fermi energy. However, the electronic density of states (DOS) several hundred eV above the Fermi energy, calculated using finite k-point grids, exhibits a highly oscillatory structure which converges extremely slowly with k-point density. For realistic k-point densities, this in turn leads to very noisy response functions in which the underlying resonance structure is obscured, making the calculation of $X^{(2)}$ at high energies impractical. In reality, the energies of excited states high above the Fermi energy are characterized by significant lifetime broadening. This fact can be utilized to effectively smooth out the density of states and mitigate numerical noise in the response function calculation. Therefore, in the same spirit as the work of Klinkusch et al. [15] in the context of photoemission, we added a heuristic energy dependent imaginary part to the unoccupied Kohn-Sham energies to take into account lifetime broadening at high energies. Accordingly, we treat unoccupied Kohn-Sham eigenstates with eigenvalues above the Fermi energy (E_F) as quasiparticle energies and set:

$$\varepsilon_m \rightarrow \varepsilon_m + i\Gamma(\varepsilon_m) \; with \; \Gamma(E) = \frac{1}{\lambda}\sqrt{E - E_F} \tag{1}$$

The imaginary part Γ(E) has a square root dependence on the energy and the λ parameter is related to the inelastic mean free path of electrons [16], which is ∼92 Å in graphite [17]. This yields a lifetime broadening of ∼0.35 eV for electronic states ∼280 eV above the Fermi energy. Incorporating the modified complex eigen-energies ε_m for the unoccupied states into the excitation frequencies ω_{mn} entering into the calculation of the second-order response functions [14] eliminates numerical noise at high energies and leads to numerical convergence of $X^{(2)}_{zzz}(2\omega, \omega, \omega)$ with k-point sampling density. The broadening in the calculated spectra only assumes lifetime (virtual state: 0.35 eV, core-hole: 0.1 eV) and thermal broadening (0.25 eV). The thermal broadening is based on the average fluctuations in the atomic positions from *ab initio* molecular dynamics simulations of an eight-layer graphite slab. Experimental spectra will be broadened significantly by sample imperfections, atomic motions and experimental conditions.

SHG generally requires inversion symmetry to be broken on the length scale of the incident radiation [18]. As bulk graphite has an inversion center, it should exhibit no second harmonic response. Inversion symmetry is broken at the surface of graphite however, and we expect some SHG. In the real world experiment, on a sample of finite thickness, light is incident on the top surface of the sample and the bottom surface at the other end of the sample is effectively at infinity. Lack of inversion symmetry at the top surface which responds to the field leads to SHG. On the other hand, in the slab supercell set up considered here, the system effectively responds to a spatially homogeneous electric field that acts at both surfaces of the slab and the system as a whole exhibits inversion symmetry regardless of the number of graphene layers in the slab. The second-order response from one surface cancels that from the other surface leading to overall signal attenuation. Therefore, in order to describe SHG resulting from the loss of inversion symmetry at the top surface, only one of the two surfaces needs to be active in the simulation. This is achieved for the case of core electron response by only considering the C $1s$ electronic states on C atoms in the top four layers of the eight-layer slab explicitly in the valence self-consistent field procedure. For the bottom four layers, the C $1s$ electronic states are treated implicitly by including them in the core; these states do not enter the second-order response calculation. In Fig. S4, we show the C $1s$ contribution to the absolute magnitude $|X^{(2)}_{zzz}(2\omega, \omega, \omega)|$ of the zzz component of the second harmonic susceptibility over an extended energy range. At ∼132 eV, which corresponds to half the Kohn-Sham C $1s \rightarrow$ conduction band excitation energy in graphite, an edge onset is apparent in $|X^{(2)}|$. Interestingly, although

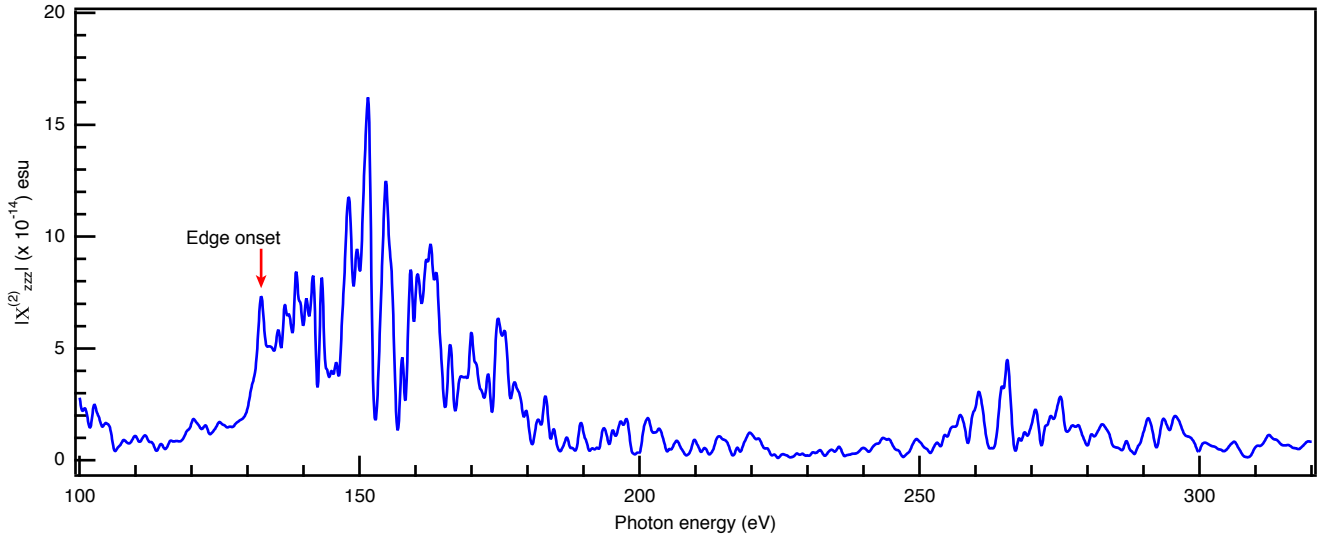

FIG. S4: Extended Range SH response. Calculated C $1s$ contribution to the absolute magnitude $|X^{(2)}_{zzz}(2\omega, \omega, \omega)|$ of the zzz component of the second harmonic susceptibility over an extended energy range. An edge onset is apparent in $|X^{(2)}_{zzz}|$ at ∼132 eV, which corresponds to half the Kohn-Sham C $1s \rightarrow$ conduction band excitation energy in graphite (∼264 eV in the theory). Note that for the theoretical spectra, presented in Fig. 3, a rigid shift of 20 eV was applied.

some signal enhancement is also observed near 270 eV, the magnitude of the SHG response is higher at ω near half the C K edge energy than near the edge itself. This suggests that in this instance, the contribution to from the 2ω resonance terms is stronger than the ω resonance terms [14]. Note that in LDA the C $1s$ core state binding energies are underestimated by roughly 20 eV. Therefore, in order to align the energy axis with experiment, a rigid shift of 20 eV is applied to the spectra shown in Fig. 3. The exponential decay observed in the magnitude of the SHG response with increasing layer depth shown in Fig. 3(c) indicates that an eight-layer slab is sufficient to simulate SHG at the graphite surface.

[1] A. Simoncig, R. Mincigrucci, E. Principi, F. Bencivenga, A. Calvi, L. Foglia, G. Kurdi, L. Raimondi, M. Manfredda, N. Mahne, R. Gobessi, S. Gerusina, C. Fava, M. Zangrando, A. Matruglio, S. Dal Zilio, V. Masciotti, and C. Masciovecchio, in *Proc. SPIE*, Vol. 10243, edited by A. Klisnick and C. S. Menoni (2017) p. 102430L.

[2] C. Masciovecchio, A. Battistoni, E. Giangrisostomi, F. Bencivenga, E. Principi, R. Mincigrucci, R. Cucini, A. Gessini, F. D'Amico, R. Borghes, M. Prica, V. Chenda, M. Scarcia, G. Gaio, G. Kurdi, A. Demidovich, M. B. Danailov, A. Di Cicco, A. Filipponi, R. Gunnella, K. Hatada, N. Mahne, L. Raimondi, C. Svetina, R. Godnig, A. Abrami, and M. Zangrando, Journal of Synchrotron Radiation **22**, 553 (2015).

[3] E. Allaria, R. Appio, L. Badano, W. Barletta, S. Bassanese, S. Biedron, A. Borga, E. Busetto, D. Castronovo, P. Cinquegrana, S. Cleva, D. Cocco, M. Cornacchia, P. Craievich, I. Cudin, G. D'Auria, M. Dal Forno, M. Danailov, R. De Monte, G. De Ninno, P. Delgiusto, A. Demidovich, S. Di Mitri, B. Diviacco, A. Fabris, R. Fabris, W. Fawley, M. Ferianis, E. Ferrari, S. Ferry, L. Froehlich, P. Furlan, G. Gaio, F. Gelmetti, L. Giannessi, M. Giannini, R. Gobessi, R. Ivanov, E. Karantzoulis, M. Lonza, A. Lutman, B. Mahieu, M. Milloch, S. Milton, M. Musardo, I. Nikolov, S. Noe, F. Parmigiani, G. Penco, M. Petronio, L. Pivetta, M. Predonzani, F. Rossi, L. Rumiz, A. Salom, C. Scafuri, C. Serpico, P. Sigalotti, S. Spampinati, C. Spezzani, M. Svandrlik, C. Svetina, S. Tazzari, M. Trovo, R. Umer, A. Vascotto, M. Veronese, R. Visintini, M. Zaccaria, D. Zangrando, and M. Zangrando, Nat. Photonics **6**, 699 (2012).

[4] E. Allaria, D. Castronovo, P. Cinquegrana, P. Craievich, M. Dal Forno, M. B. Danailov, G. D'Auria, A. Demidovich, G. De Ninno, S. Di Mitri, B. Diviacco, W. M. Fawley, M. Ferianis, E. Ferrari, L. Froehlich, G. Gaio, D. Gauthier, L. Giannessi, R. Ivanov, B. Mahieu, N. Mahne, I. Nikolov, F. Parmigiani, G. Penco, L. Raimondi, C. Scafuri, C. Serpico, P. Sigalotti, S. Spampinati, C. Spezzani, M. Svandrlik, C. Svetina, M. Trovo, M. Veronese, D. Zangrando, and M. Zangrando, Nat. Photonics **7**, 913 (2013).

[5] P. Finetti, H. Höppner, E. Allaria, C. Callegari, F. Capotondi, P. Cinquegrana, M. Coreno, R. Cucini, M. B. Danailov, A. Demidovich, G. De Ninno, M. Di Fraia, R. Feifel, E. Ferrari, L. Fröhlich, D. Gauthier, T. Golz, C. Grazioli, Y. Kai,

G. Kurdi, N. Mahne, M. Manfredda, N. Medvedev, I. P. Nikolov, E. Pedersoli, G. Penco, O. Plekan, M. J. Prandolini, K. C. Prince, L. Raimondi, P. Rebernik, R. Riedel, E. Roussel, P. Sigalotti, R. Squibb, N. Stojanovic, S. Stranges, C. Svetina, T. Tanikawa, U. Teubner, V. Tkachenko, S. Toleikis, M. Zangrando, B. Ziaja, F. Tavella, and L. Giannessi, Phys. Rev. X **7**, 021043 (2017).

[6] M. Zangrando, D. Cocco, C. Fava, S. Gerusina, R. Gobessi, N. Mahne, E. Mazzucco, L. Raimondi, L. Rumiz, and C. Svetina, J. Synchrotron Radiat. **22**, 565 (2015).

[7] L. Poletto, F. Frassetto, P. Miotti, A. Di Cicco, P. Finetti, C. Grazioli, F. Iesari, A. Kivimäki, S. Stagira, and M. Coreno, Rev. Sci. Instrum. **85**, 103112 (2014).

[8] P. Hohenberg and W. Kohn, Phys. Rev. **136**, B864 (1964).

[9] W. Kohn and L. J. Sham, Phys. Rev. **140**, A1133 (1965).

[10] A. Gulans, S. Kontur, C. Meisenbichler, D. Nabok, P. Pavone, S. Rigamonti, S. Sagmeister, U. Werner, and C. Draxl, J. Phys. Condens. Matter **26**, 363202 (2014).

[11] P. Trucano and R. Chen, Nature **258**, 136 (1975).

[12] N. Ooi, A. Rairkar, and J. B. Adams, Carbon **44**, 231 (2006).

[13] J. P. Perdew and A. Zunger, Phys. Rev. B **23**, 5048 (1981).

[14] S. Sharma and C. Ambrosch-Draxl, Phys. Scr. **T109**, 128 (2004).

[15] S. Klinkusch, P. Saalfrank, and T. Klamroth, J. Chem. Phys. **131**, 114304 (2009).

[16] A. P. Sorini, J. J. Kas, J. J. Rehr, M. P. Prange, and Z. H. Levine, Phys. Rev. B **74**, 165111 (2006).

[17] C. Kunz, B. Cowie, W. Drube, T.-L. Lee, S. Thiess, C. Wild, and J. Zegenhagen, J. Electron Spectros. Relat. Phenomena **173**, 29 (2009).

[18] A. Nazarkin, S. Podorov, I. Uschmann, E. Förster, and R. Sauerbrey, Phys. Rev. A **67**, 41804 (2003).